Stabilized Macro Basis Function MoM for Wideband Analysis of Wire Coupling

William R. Dommisse[1], Matthys M. Botha[2], Thomas Rylander[3] and Jan Carlsson[4]

[1] Dept. of Electrical and Electronic Engineering, Stellenbosch Univ., Stellenbosch 7600, South Africa
[2] Dept. of Electrical and Electronic Engineering, Stellenbosch Univ., Stellenbosch 7600, South Africa
[3] Dept. of Electrical Engineering, Chalmers Univ. of Tech., Göteborg, SE-412 96, Sweden
[4] Provinn AB, Göteborg, SE-411 05, Sweden.

Abstract

This article presents a macro basis function (MBF) set to represent wire surface currents in the method of moments (MoM), for full-wave computational electromagnetic modeling of complex wire coupling effects over broad frequency ranges. Such modeling is important for design and operational characterization of systems relying on wires for data and power transmission, where it is necessary to ensure that electromagnetic interference (EMI) is acceptably low to maintain electromagnetic compatibility (EMC). The MBFs allow for both axial and circumferential components and variations. They are constructed from standard MoM basis functions for representing surface current density on triangle element meshes, resulting in significantly fewer unknowns. The MBFs build on a previously proposed set. They are reformulated to ensure that solenoidal current flow can be exactly represented, thereby eradicating the occurrence of spurious solutions. This enables stable, accurate and efficient wideband analysis, as demonstrated with crosstalk and radiated immunity results for various transmission line coupling test cases. For these applications it is found that existing methods tailored to wire coupling analysis, namely thin-wire MoM and hybrid transmission line theory (TLT) solvers, are generally not reliable.

Keywords: crosstalk, irradiation, junction, macro basis functions, method of moments, multiscale, proximity effect, radiation, spurious modes, wire antenna

The work of W. R. Dommisse and M. M. Botha was supported in part by the South African Radio Astronomy Observatory (SARAO) and in part by the South African National Research Foundation under Grant 75322. The work of T. Rylander and J. Carlsson was supported in part by the FFI MORFex project, which is partly funded by the Swedish Energy Agency.

1 Introduction

Wires are an essential component in wide-ranging modern systems for data and power transmission between various components, e.g. sensors, motors, controllers, antennas, etc., covering a very broad frequency range. Application domains are diverse, e.g. automotive, aerospace, and communication systems. Depending on operating environment and structural considerations, the effort required to ensure that electromagnetic interference (EMI) is at acceptably low levels to maintain electromagnetic compatibility (EMC), may vary [1, 2]. In some instances, effects of intentional EMI (IEMI) must also be considered [3, 4]. Thus, for design and operational characterization, computational modeling of complex wire proximity and radiative effects is important [5, 6]. This article presents a set of macro basis functions (MBFs) to represent surface current density on wires, for accurate and efficient method of moments (MoM) modeling of perfect electrical conductor (PEC) wire geometries over wide frequency bands. These MBFs are a stabilized evolution of the formulation presented in [7] for electrically thick wires, with the latter set shown to be unsuitable for wideband applications that include the electrically very thin regime, due to occurrence of spurious solutions. To assess solver performance, a range of transmission line (TL) test geometries are considered, which include strong coupling effects.

When wire proximity and radiative effects are significant, the MoM is a natural choice for full-wave modeling because of the exact representation of basis functions' radiated fields. Development of MoM formulations for wires has received much attention in the research literature over many years. Overviews of various progressive approaches and considerations are provided in e.g. [7, 8, 9, 10], with the current industry standard being the well-known exact-kernel, thin-wire, electric field integral equation (EFIE) based MoM formulation, employing tubular rooftop basis functions which allow only for circumferentially invariant axial current flow [11, 12, 13, 14, 15]. When modeling TLs with wires in close proximity to each other or to ground, the thin-wire MoM may become inaccurate due to the noted restriction brought by the rooftop basis. In such cases, solvers based on transmission line theory (TLT) may be preferred [16, 17]. Extensions to standard TLT models to account for radiation, irradiation and coupling effects have been formulated; see e.g. [5, 18, 19, 20, 21, 22] and the references therein. The extensions most often involve a two-step hybrid approach. E.g. for irradiation analysis, the external field problem containing the aggressor source, is solved with a conventional full-wave solver, such as the MoM or finite element method (FEM), without the victim TL present. This solution field sampled along the TL path is then used as a distributed impressed source, serving as excitation to the TLT based solution of the TL. For coupling between TLs, the aggressor's current distribution may be solved first with TLT, and then used as impressed source for two-step irradiation analysis of the victim TL. Clearly, such a sequential procedure does not account for bidirectional coupling effects and thus is not a true full-wave solution. Additionally, the accuracy of the approximation is often limited by the TLT's range of applicability, i.e. wires must run at an electrically small distance from their reference conductor, wire lengths must be substantially larger than this distance [5], and circuit models must be available to represent terminations. In spite of these limitations, the approximate hybrid approach is offered in various commercial solver suites, such as FEKO [23], CST [24] and EMEC [25], due to its efficiency, and in the absence of true full-wave formulations which are efficient for these challenging multiscale problems.

Currently, an accurate full-wave solution that properly accounts for wire coupling effects is only achievable by employing a general full-wave solver for PEC surfaces in three dimensions, such as the ubiquitous EFIE-based MoM with Rao-Wilton-Glisson (RWG) basis functions [26]. The latter is indeed used here as reference solution; however, it becomes prohibitively expensive for practical application to complex wire geometries. This finally leads to using MBFs to represent wire surface current flow with greatly reduced degrees of freedom (DoFs) compared to the RWG MoM, while still yielding an accurate full-wave solution [7]. MBFs are formed as fixed linear combinations of low-level basis functions (LBFs), which represent physically expected current flows over larger supports than individual LBFs, leading to reduced DoFs [27, 28]. As noted above, the formulation of [7] is the starting point for the work presented here, which addresses deficiencies for wideband analysis.

Section 2 reviews relevant details of the existing wire MBF MoM formulation from [7]. Section 3 first investigates the occurrence of spurious solutions in the existing formulation and discusses their origin. Second, it provides a stabilization solution, by which the MBFs are altered such that solenoidal current flows can be represented exactly. This is the main theoretical contribution of the article. Section 4 presents wideband crosstalk and radiated immunity results; the stabilized MBF solver is compared to commercial thin-wire MoM and hybrid TLT solvers. It is found that in some cases, neither of these commercial solutions tailored to wire analysis can produce accurate results. Section 5 concludes the article.

2 Summary of Existing Wire MBF Formulation

The underlying LBF MoM formulation is first described, followed by the procedure for DoF reduction through MBFs, and then the MBFs themselves.

2.1 Wire Surface Mesh and LBF MoM System

A wire is represented with a structured triangular mesh following a contour path. The mesh consists of conformal tubular segments, each circumferentially discretized uniformly into K flat quadrilateral panels, with each panel divided into two triangles; as shown in various figures, see e.g. Fig. 1. Upon this mesh, a Galerkin tested EFIE based MoM [26], employing full first-order basis functions [29, 30], is formulated. This means that with each shared edge two basis functions are associated: an RWG and a solenoidal one. These are the LBFs. The resulting system of linear equations is

$$\mathbf{ZJ} = \mathbf{V} \tag{1}$$

where $\mathbf{Z}$ is the $N \times N$ impedance matrix, $\mathbf{V}$ is the $N \times 1$ excitation vector, and $\mathbf{J}$ is the $N \times 1$ current coefficient vector, i.e. the DoFs to be solved, where N

denotes the number of LBFs. The entries are defined as

$$Z_{mn} = jk_0 Z_0 \int_S \int_S \boldsymbol{b}_m(\boldsymbol{r}) \cdot \boldsymbol{b}_n(\boldsymbol{r}')\, G_0 \, dS' dS$$
$$- \frac{jZ_0}{k_0} \int_S \int_S \nabla_s \cdot \boldsymbol{b}_m(\boldsymbol{r}) \nabla'_s \cdot \boldsymbol{b}_n(\boldsymbol{r}')\, G_0 \, dS' dS \tag{2}$$

$$V_m = \int_S \boldsymbol{b}_m(\boldsymbol{r}) \cdot \boldsymbol{E}_{\text{inc}} \, dS, \tag{3}$$

where Z_0 is the free space wave impedance, k_0 is the free space wavenumber, $G_0(\boldsymbol{r}, \boldsymbol{r}') = e^{-jk_0|\boldsymbol{r}-\boldsymbol{r}'|}/(4\pi|\boldsymbol{r} - \boldsymbol{r}'|)$ is the free space Green's function, and $\boldsymbol{b}_m$ is the mth LBF.

2.2 Wire MBF Reduced MoM System

Consider the general case of a surface constituted of both wire and non-wire parts. Upon non-wire parts the LBFs are employed to represent the surface current density, $\boldsymbol{J}$, while upon wire parts MBFs are employed. The MBFs are fixed linear combinations of LBFs, such that they describe the wire currents with much fewer DoFs. The overall representation is

$$\boldsymbol{J} = \sum_{n=1}^{N_{\boldsymbol{b}}} J_n \boldsymbol{b}_n + \sum_{n=N_{\boldsymbol{b}}+1}^{N_{\boldsymbol{b}}+N_{\boldsymbol{B}}} J_n \boldsymbol{B}_{n-N_{\boldsymbol{b}}}, \tag{4}$$

where $\boldsymbol{B}_m$ is the mth MBF, $N_{\boldsymbol{b}}$ is the number of LBF DoFs on external geometry and $N_{\boldsymbol{B}}$ is the number of wire MBF DoFs. The reduced system follows as

$$\mathbf{Z}_{\text{red}} \mathbf{J}_{\text{red}} = \mathbf{V}_{\text{red}} \tag{5}$$

$$\mathbf{Z}_{\text{red}} = \mathbf{B}^H \mathbf{Z} \mathbf{B}, \quad \mathbf{V}_{\text{red}} = \mathbf{B}^H \mathbf{V}. \tag{6}$$

where $\mathbf{B}$ is the basis function definition matrix. Columns $1, ..., N_{\boldsymbol{b}}$ are as the identity matrix, and columns $N_{\boldsymbol{b}} + 1, ..., N_{\boldsymbol{b}} + N_{\boldsymbol{B}}$ contain the fixed LBF coefficients forming the MBFs.

2.3 Construction of Wire MBFs

The wire surface consists of the tubular segments and end-caps. The reference segment with radius a and axial length 1, is parameterized by cylindrical coordinates (ρ, φ, ℓ), as $\rho = a$, $\varphi \in [0, 2\pi]$, and $\ell \in [0, 1]$. Upon the reference segment, nine MBFs are analytically defined, representing axial and circumferential current flow, as

$$\boldsymbol{B}_{\text{axi}} = \begin{cases} \ell \Phi_i(\varphi) \hat{\ell} \\ (1 - \ell) \Phi_i(\varphi) \hat{\ell} \end{cases} \tag{7}$$

$$\boldsymbol{B}_{\text{cir}} = \Phi_i(\varphi) \hat{\varphi} \tag{8}$$

with

$$\Phi_1(\varphi) = 1, \quad \Phi_2(\varphi) = \cos \varphi, \quad \Phi_3(\varphi) = \sin \varphi, \tag{9}$$

where $\hat{\rho}$, $\hat{\ell}$ and $\hat{\varphi}$ are the base vectors of the coordinate system. This set consists of the conventional thin-wire MoM's axial rooftop basis functions, plus circumferential current representation, and modeling up to first-order harmonic circumferential variation. In (7) the top expression describes rooftop functions associated with the segment's end node; the bottom expression describes those associated with its start node.

The reference end-cap is parameterized by cylindrical coordinates (ρ, φ), as $\rho \in [0, a]$ and $\varphi \in [0, 2\pi]$. Six end-cap MBFs are analytically defined, representing radial and azimuthal current flow, as

$$\boldsymbol{B}_{\text{rad}} = \pm \begin{cases} \dfrac{\rho}{a}\Phi_1(\varphi)\hat{\rho} \\ \Phi_2(\varphi)\hat{\rho} - \Phi_3(\varphi)\hat{\varphi} \\ \Phi_3(\varphi)\hat{\rho} + \Phi_2(\varphi)\hat{\varphi}. \end{cases} \tag{10}$$

$$\boldsymbol{B}_{\text{azi}} = \frac{\rho}{a}\Phi_i(\varphi)\hat{\varphi}. \tag{11}$$

These functions are analytically mapped onto the actual segment and end-cap domains, using contravariant component transformations that maintain divergence conformity (see [7]). This allows for tapered and untapered wires and segments joined at any angle.

After mapping, the MBFs are analytically defined on the tubular segments and circular disks, described in the mesh by triangle elements. Thus, the final step is to project every MBF onto a LBF representation, yielding the latter columns of $\mathbf{B}$ in (6). This projection is accomplished on an edge-by-edge basis, by linearly interpolating the in-surface normal components of the analytical MBFs along each edge [7], since the full first-order LBFs have the capability of representing linear variation of normal components along each shared mesh edge.

Lastly, at connections of wires to external geometry, junction MBFs for continuous axial current flow are employed, as fully described in [7].

3 Stabilized Wire MBFs

The formulation presented in [7] is aimed at wires of appreciable electrical thickness, where it is noted that spurious solutions are encountered for sufficiently electrically thin wires. This section starts by confirming the onset of spurious solutions as the wire radius is reduced. A stabilization scheme which eradicates the occurrence of spurious solutions is then presented, thereby removing the wire radius limitation on MBF applicability.

3.1 Spurious Solutions Investigation

Consider the simple test case of a $\lambda/2$ long wire in free space, excited by a 300 MHz plane wave, with incidence direction orthogonal to the wire axis (λ is the free-space wavelength). There is no external geometry. Three MoM solutions are found, namely using the LBFs ($\mathbf{J}$, N coefficients), using RWG basis functions (the mixed first-order subset of LBFs [7], $\mathbf{J}_{\text{RWG}}$, $N/2$ coefficients),

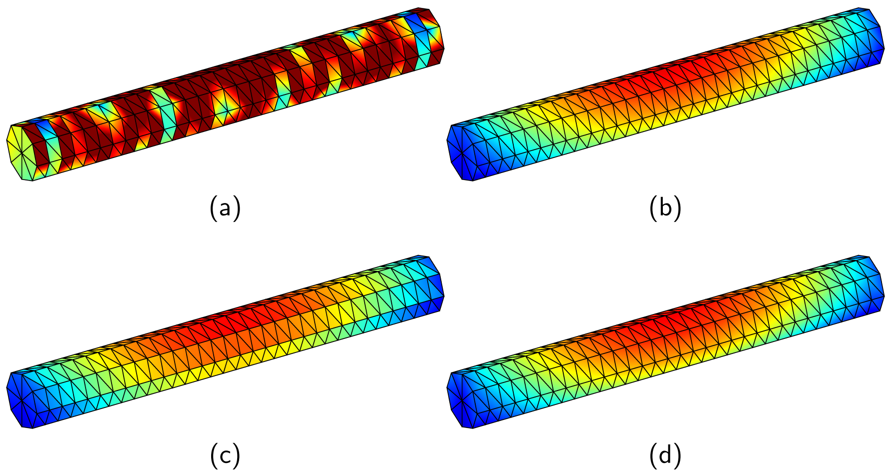

Figure 1: Instantaneous surface current density for a $\lambda/2$ wire illuminated by a plane wave: (a) solution $\mathbf{J}_{\text{red}}$, using the existing MBF formulation [7], (b) solution $\mathbf{J}_{\text{PFO}}$, (c) solution $\mathbf{J}_{\text{RWG}}$, (d) solution $\mathbf{J}$.

and using the existing wire MBFs of [7] ($\mathbf{J}_{\text{red}}$, $N_{\boldsymbol{B}}$ coefficients). To assess the capability of the existing MBFs to represent the LBF solution, the latter can be projected onto the MBF space, as $\mathbf{J}_{\text{PFO}} = (\mathbf{B}^H\mathbf{B})^{-1}\mathbf{B}^H\mathbf{J}$, with PFO standing for "projected full order." Fig. 1 visualizes these currents for the case of $a = \lambda/20$, with the incident electric field polarized parallel to the wire axis. It shows that the LBF and RWG solutions yield entirely similar and physically expected, correct results. The MBF solution is clearly spurious. However, when approximating the physically correct LBF solution with a linear combination of the MBFs via projection, the resulting current $\mathbf{J}_{\text{PFO}}$ is visually indistinguishable from $\mathbf{J}$. Therefore, the MBFs do have the functional capability to represent the physically correct solution well.

To quantitatively assess this spurious solution phenomenon over a broader range, consider both parallel and orthogonally polarized incident waves, as well as two circumferential discretizations, $K = \{8, 16\}$, over the radius range $a/\lambda \in [10^{-3}, 10^{-1}]$, which can be considered electrically very thin to quite thick. Measure the MBF solution's percentage relative error using the Frobenius norm, as

$$\text{Error} = \frac{||\mathbf{J}_{\text{red}} - \mathbf{J}_{\text{PFO}}||_F}{||\mathbf{J}_{\text{PFO}}||_F} \times 100\%. \tag{12}$$

Fig. 2 shows the results, indicating that the spurious solutions are absent for sufficiently thick wires, for which the MBF solutions are accurate and efficient, as demonstrated in [7]. However, the onset of spurious solutions at sufficiently small radii poses a problem for wideband analysis. In fact, for the lower value of $K = 8$ the onset occurs at $a \approx 0.07\lambda$, which is electrically fairly thick. It is seen that by increasing K the electrical radius of onset can be reduced but cannot be eliminated entirely.

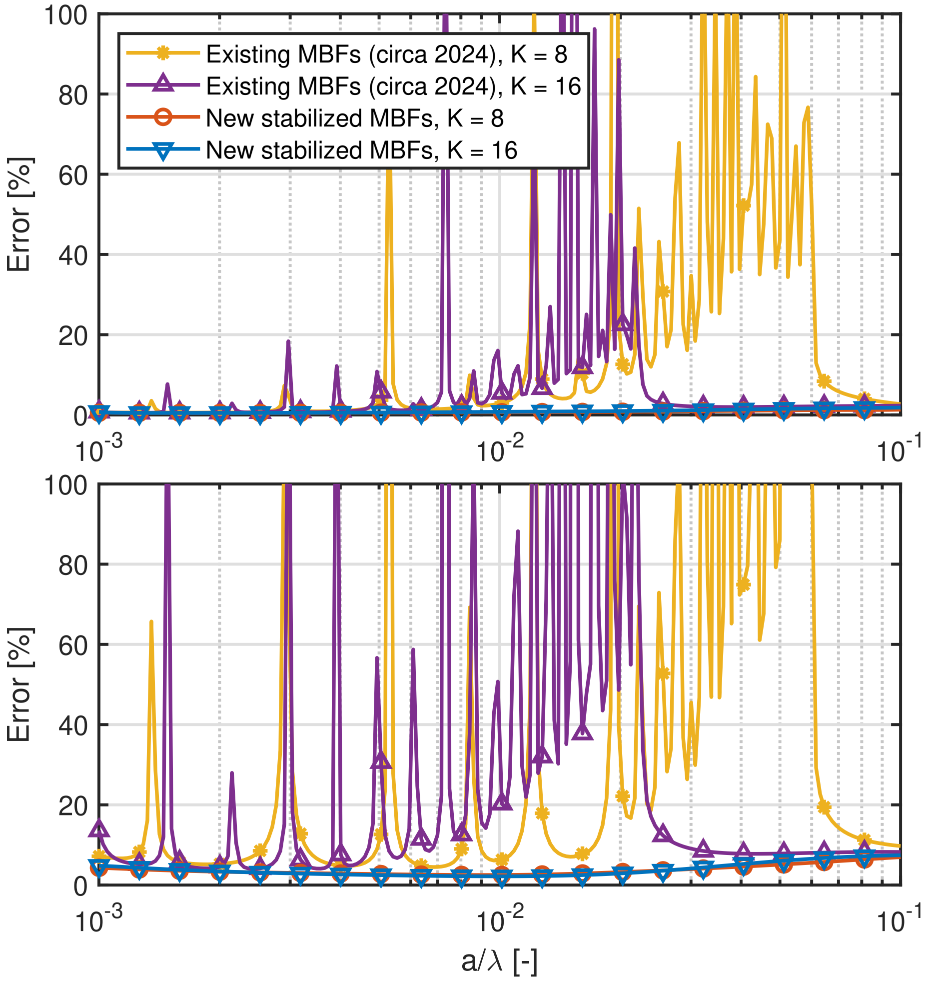

Figure 2: Percentage relative error in MBF solutions for scattering analysis of a $\lambda/2$ wire, as the radius is varied. Two polarizations of the incident electric field are considered, as well as two circumferential mesh densities. Top: parallel to the wire axis. Bottom: orthogonal to the wire axis.

3.2 Discussion

The problem of spurious solutions is well known in the FEM community, which occurs when unsuitable bases are used to solve the vector wave equation (VWE) [31, 32, 33, 34]. The weak form of the VWE features two terms: the *curl term* is proportional to the curl of the field and the *linear term* is proportional to the field itself. When the basis cannot properly represent the null space of the curl operator (i.e. gradient fields), then the curl term cannot be properly set to zero, leading to poor enforcement of Gauss' law (for an electric field formulation). This causes non-physical (spurious) components to appear in the solution. Another way of viewing this is simply that when the formulation is constrained in its ability to set the curl term to arbitrarily small values, then non-physical compensation takes place via the linear term. The latter perspective is con-

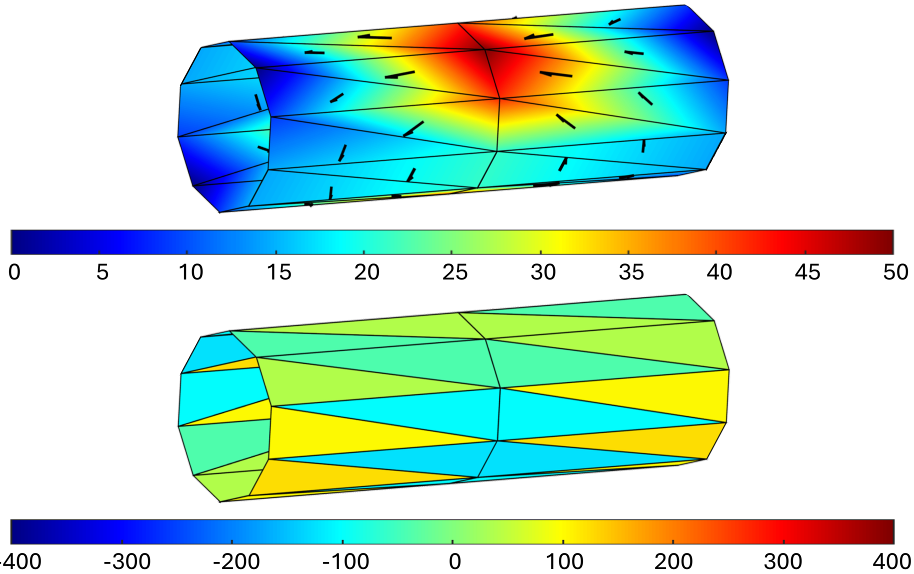

Figure 3: Linear combination of MBFs realized with the existing formulation [7], to represent solenoidal flow. Top: MBFs. Bottom: divergence of MBFs.

structive in the MoM context. In (2) there is the scalar potential term, which is proportional to the surface divergence of the current (i.e. the charge), and the vector potential term, which is directly proportional to the current itself. Should the basis not allow for setting the charge to arbitrarily small values for nonzero $\boldsymbol{J}$, then spurious solutions may result. Thus, the MBFs should be capable of representing solenoidal currents. To assess this, consider the sum of a sinusoidally-varying axial rooftop MBF and two cosinusoidally-varying circumferentially-directed MBFs. With appropriate scaling, the analytical definitions (7) and (8) sum up to a solenoidal current distribution. However, Fig. 3 shows that the LBF realization does not yield identically zero surface divergence. This is the fundamental reason for the spurious solutions. It is surmised that the spurious solutions only occur at sufficiently small radii, due to increasingly strong local coupling with the spurious charges. For higher K values, the onset radius is smaller, since such MBFs resemble the analytical forms more closely.

3.3 Stabilization

To stabilize the MBFs, the LBF-based realization of the analytical forms must be revisited, such that for every non-solenoidal MBF, another MBF can be added to it to yield solenoidal flow on a given tubular segment. This is analogous to how the LBFs can achieve zero divergence on a given triangle, since each RWG's divergence forms a piecewise-constant charge doublet with zero net charge, which can be canceled out on a given triangle by adding an appropriately scaled RWG associated with another edge of that triangle. The second LBF per shared edge does not play a role in representing divergent current flow since it is solenoidal.

First construct a *proto-MBF* out of RWGs, which forms a charge doublet over two quadrilateral panels sharing an edge in the wire surface mesh (see Sec. 2.1). This step is motivated by the fact that all MBF supports are collections of such quadrilaterals. The proto-MBF is a building block for constructing MBFs with charges canceling out on a given segment, as described next.

3.3.1 Proto-MBF

Each quadrilateral pair consists of four triangles, as shown in Fig. 4, labeled T_1 to T_4. The proto-MBF is formed on this domain, as a linear combination of the three RWGs associated with the shared edges, numbered $1, 2, 3$ in the figure. Let $\{\boldsymbol{b}_1, \boldsymbol{b}_2, \boldsymbol{b}_3\}$ and $\{c_1, c_2, c_3\}$ denote the corresponding RWGs and their intermediate coefficients, respectively. These three coefficients are computed from three charge-doublet requirements, namely that the total charge on quadrilateral 1 ($T_1 \cup T_2$) be Q, the total charge on quadrilateral 2 ($T_3 \cup T_4$) be $-Q$, and that the charge densities are constant on each quadrilateral. Based on the definition of the RWG function [7], coefficients c_1 and c_3 can be calculated immediately, as

$$\begin{aligned} \nabla_s \cdot (c_1 \boldsymbol{b}_1) &= \frac{L_1}{A_1} c_1 = -j\omega \frac{Q}{A_1 + A_2} \\ \Rightarrow \quad c_1 &= -j\omega \left(\frac{A_1}{L_1} \right) \left(\frac{Q}{A_1 + A_2} \right) \end{aligned} \tag{13}$$

$$\begin{aligned} \nabla_s \cdot (c_3 \boldsymbol{b}_3) &= \frac{L_3}{A_4} c_3 = j\omega \frac{Q}{A_3 + A_4} \\ \Rightarrow \quad c_3 &= j\omega \left(\frac{A_4}{L_3} \right) \left(\frac{Q}{A_3 + A_4} \right) \end{aligned} \tag{14}$$

where A_1 to A_4 are the areas of the triangles and L_1 to L_3 are the lengths of the three RWG-associated edges. With these coefficients in place, c_2 is calculated to ensure that the requirements are also fulfilled on T_2 (and by implication on T_3), as

$$\begin{aligned} \nabla_s \cdot (c_1 \boldsymbol{b}_1 + c_2 \boldsymbol{b}_2) &= -\frac{L_1}{A_2} c_1 + \frac{L_2}{A_2} c_2 = -j\omega \frac{Q}{A_1 + A_2} \\ \Rightarrow \quad c_2 &= -j\omega \frac{Q}{L_2}. \end{aligned} \tag{15}$$

The final proto-MBF associated with the quadrilateral pair's shared edge, is obtained by normalizing the sum $c_1\boldsymbol{b}_1 + c_2\boldsymbol{b}_2 + c_3\boldsymbol{b}_3$ by c_2, such that the normal component at this edge is equal to the reciprocal of its length (i.e. $1/L_2$), as

$$\boldsymbol{P} = \frac{c_1}{c_2} \boldsymbol{b}_1 + \boldsymbol{b}_2 + \frac{c_3}{c_2} \boldsymbol{b}_3. \tag{16}$$

This is now independent of the intermediate charge Q, used in its construction. Fig. 4 visualizes $\boldsymbol{P}$ and $\nabla_s \cdot \boldsymbol{P}$, confirming the desired properties.

3.3.2 MBF Construction Along Wires

The discretized MBFs are constructed as fixed linear combinations of K proto-MBFs, either associated with circumferential edges (for axial MBFs) or axial edges (for circumferential MBFs) together with a linear combination of

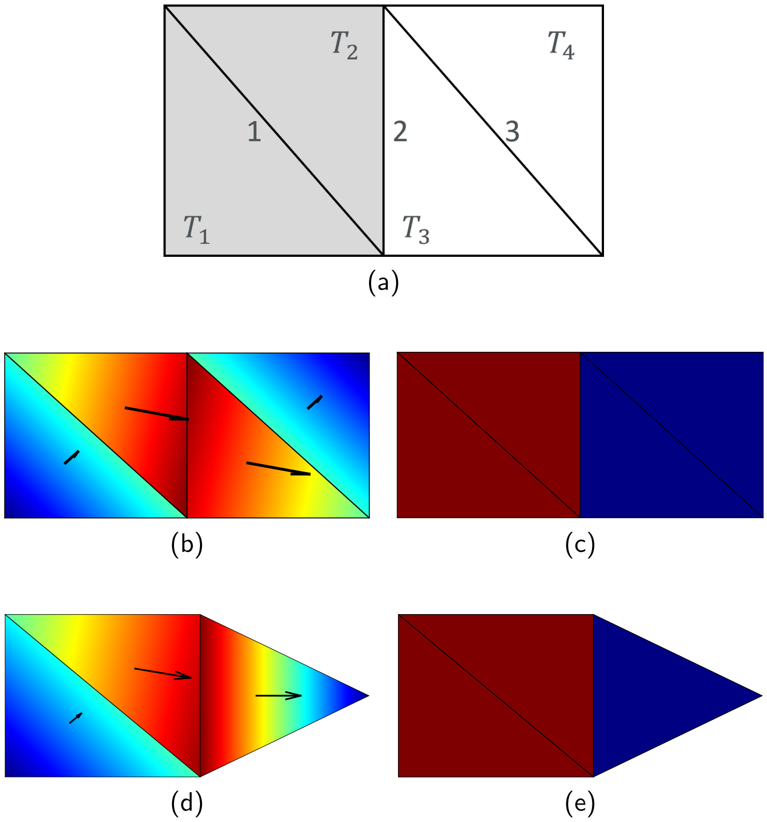

Figure 4: Proto-MBF properties. (a) Quadrilateral pair with shared edge and triangle labels. (b) Magnitude and direction of quadrilateral pair proto-MBF. (c) Divergence of quadrilateral pair proto-MBF. (d) Magnitude and direction of end-cap proto-MBF. (e) Divergence of end-cap proto-MBF.

solenoidal LBFs, $\boldsymbol{B}_n^{\mathrm{sol}}$, as

$$\boldsymbol{B}_n = \boldsymbol{B}_n^{\mathrm{sol}} + \sum_{k=1}^{K} p_k \boldsymbol{P}_k, \tag{17}$$

where p_k is the proto-MBF coefficient and k is the circumferential/axial edge with which $\boldsymbol{P}_k$ is associated.

To ensure the desired MBF properties stated at the beginning of this section, it is required that analytical MBFs' total current flows across quadrilateral edges are consistently replicated by the discrete ones. The component $\boldsymbol{B}_n^{\mathrm{sol}}$ is not relevant to this objective, as it does not contribute to total current flow across any mesh edge, since, by construction, the solenoidal LBFs describe net zero current flow across mesh edges. For the axial MBFs associated with a junction between two segments (also referred to as a node), which is formed by an elliptic arc, the proto-MBF coefficients are set equal to the total axially directed current across the junction over the angular range formed by two consecutive circumferential vertices, as

$$p_k^{\mathrm{axi}} = \int_{\varphi_k}^{\varphi_{k+1}} \Phi_i(\varphi)\, d\varphi. \tag{18}$$

Here, the differential element is actually $ad\varphi$ (in case of a circular node contour), but the transformation of (7) from reference to actual domain brings a scaling factor of $1/a$. Such exact cancellation also occurs for general elliptic node contours, thus the expression is correct. An analogous procedure applies when constructing the circumferential MBFs, with the difference that current flows across axially-directed quadrilateral edges on a segment, are matched. A given edge is located at circumferential angle φ_k, hence the associated proto-MBF coefficient follows as

$$p_k^{\mathrm{cir}} = \Phi_i(\varphi_k). \tag{19}$$

Again, when accounting for the transformation of (8) to the actual domain, it follows that (19) indeed represents the total circumferential current at φ_k. Section 3.4 demonstrates how these divergent parts sum up to yield solenoidal flows.

With the divergent parts of the MBFs fixed, it remains to establish $\boldsymbol{B}_n^{\mathrm{sol}}$. For a given MBF, this is a linear combination of solenoidal LBFs associated with triangle edges internal to the MBF's support. The purpose is to make the discrete MBF match the analytical version as closely as possible; thus, it is a refinement term. On every internal edge, Galerkin projection is used to determine the solenoidal LBF coefficient. Let $c_{\mathrm{d}}\boldsymbol{b}_{\mathrm{d}}$ and $c_{\mathrm{s}}\boldsymbol{b}_{\mathrm{s}}$ be the RWG and solenoidal LBFs and their coefficients, associated with a given internal edge. Let $\boldsymbol{B}$ denote the analytical MBF expression. Coefficient c_{d} is already known from the proto-MBF term in (17). Determine c_{s} by projection

$$\int_L (\hat{m}\cdot\boldsymbol{b}_{\mathrm{s}})\,(\hat{m}\cdot[c_{\mathrm{d}}\boldsymbol{b}_{\mathrm{d}} + c_{\mathrm{s}}\boldsymbol{b}_{\mathrm{s}}])\, dL = \int_L (\hat{m}\cdot\boldsymbol{b}_{\mathrm{s}})\,(\hat{m}\cdot\boldsymbol{B})\, dL \tag{20}$$

which yields

$$c_{\mathrm{s}} = \frac{\displaystyle\int_L (\hat{m}\cdot\boldsymbol{b}_{\mathrm{s}})\,(\hat{m}\cdot\boldsymbol{B})\, dL}{\displaystyle\int_L (\hat{m}\cdot\boldsymbol{b}_{\mathrm{s}})^2\, dL}. \tag{21}$$

The unit vector $\hat{m}$ is orthogonal to the edge L, and lies in the plane of either triangle sharing this edge (this vector is also defined in [7]). The orthogonality of the LBFs' normal components at the edge is exploited in (21). In practice, the integrals in (21) are evaluated using trapezoidal quadrature, since the analytical functions are defined on a tubular surface and not on the triangular mesh, thus only the endpoints are guaranteed to coincide. Applying trapezoidal quadrature to a quadratic function incurs a scaling error, but this error cancels out in the numerator and denominator of (21).

3.3.3 MBF Construction at End-Caps

At end-caps a segment's current flows into a circular disk, which can be thought of as a segment with it's one end collapsed to a point. This case requires a proto-MBF forming a charge doublet on a quadrilateral sharing an edge with a triangle. The mathematical details for its construction are entirely similar as before. Fig. 4 visualizes the end-cap proto-MBF and its divergence. Analogous to forming the MBFs along the wire, total axial flows onto the K end-cap sectors are matched with those of the analytical, radial end-cap MBFs. For the azimuthal end-cap MBFs, total flow between sectors is matched. Finally, solenoidal LBFs are also added for functional refinement.

3.4 Demonstration of Solenoidal Flow Representation

The axial MBFs (7) with $i = 1$, associated with the nodes of a given segment, add up to yield constant current along the segment. The circumferential MBF (8) with $i = 1$, forms a ring of current that is solenoidal by itself.

This leaves the sinusoidally scaled axial and circumferential MBFs. Fig. 5 shows that an axial MBF with $i = \{2, 3\}$, summed with oppositely signed and appropriately scaled circumferential MBFs with both $i = \{3, 2\}$ on the two segments constituting the axial MBF's support, yields solenoidal flow. For quantitative understanding of this case, consider a quadrilateral forming part of the axial MBF's support. Two proto-MBFs contribute to current flowing out of it across three sides, namely the axial MBF and one of the circumferential MBFs, as shown in Fig. 6. Form their linear combination with scaling coefficients 1 and -1, take into account transformation to the actual segment domain, and integrate the surface divergence over the quadrilateral spanning angular range $[\varphi_1, \varphi_2]$ and axial range $[0, L]$, to yield

$$\begin{aligned}
&\int_S \nabla_s \cdot \left[\boldsymbol{B}_{\text{axi}}^{(i=2)} - \boldsymbol{B}_{\text{cir}}^{(i=3)} \right] dS \\
&= \oint_C \hat{m} \cdot \left[\boldsymbol{B}_{\text{axi}}^{(i=2)} - \boldsymbol{B}_{\text{cir}}^{(i=3)} \right] dC \\
&= \int_{\varphi_1}^{\varphi_2} \frac{\cos\varphi}{a} a d\varphi - \int_0^L \frac{\sin\varphi_2 - \sin\varphi_1}{L} dl \\
&= 0.
\end{aligned} \tag{22}$$

The surface divergence theorem was used, with (18) and (19) exploited. Given that the proto-MBFs have constant divergence on a given quadrilateral, it follows from this result that the surface divergence is identically zero. Entirely similar results hold at an end-cap, with Fig. 7 visualizing the linear combination of a radial end-cap MBF and circumferential segment MBF, yielding solenoidal flow. The sinusoidally varying azimuthal end-cap MBFs are divergent by nature, representing polarization of the end-cap disk. As such, their divergence can only be set to zero through their solution DoFs.

Finally, it is seen in the error current plots of Fig. 2, that the stabilized MBFs yield physically consistent solutions free of spurious artifacts. End-cap MBFs do not feature in the TL geometries considered further.

4 Results

To assess the stabilized wire MBF MoM's performance, wideband analysis of four TL problems of varying complexity is considered. It is compared with two commercial solvers tailored to wire analysis. Firstly, the standard exact-kernel

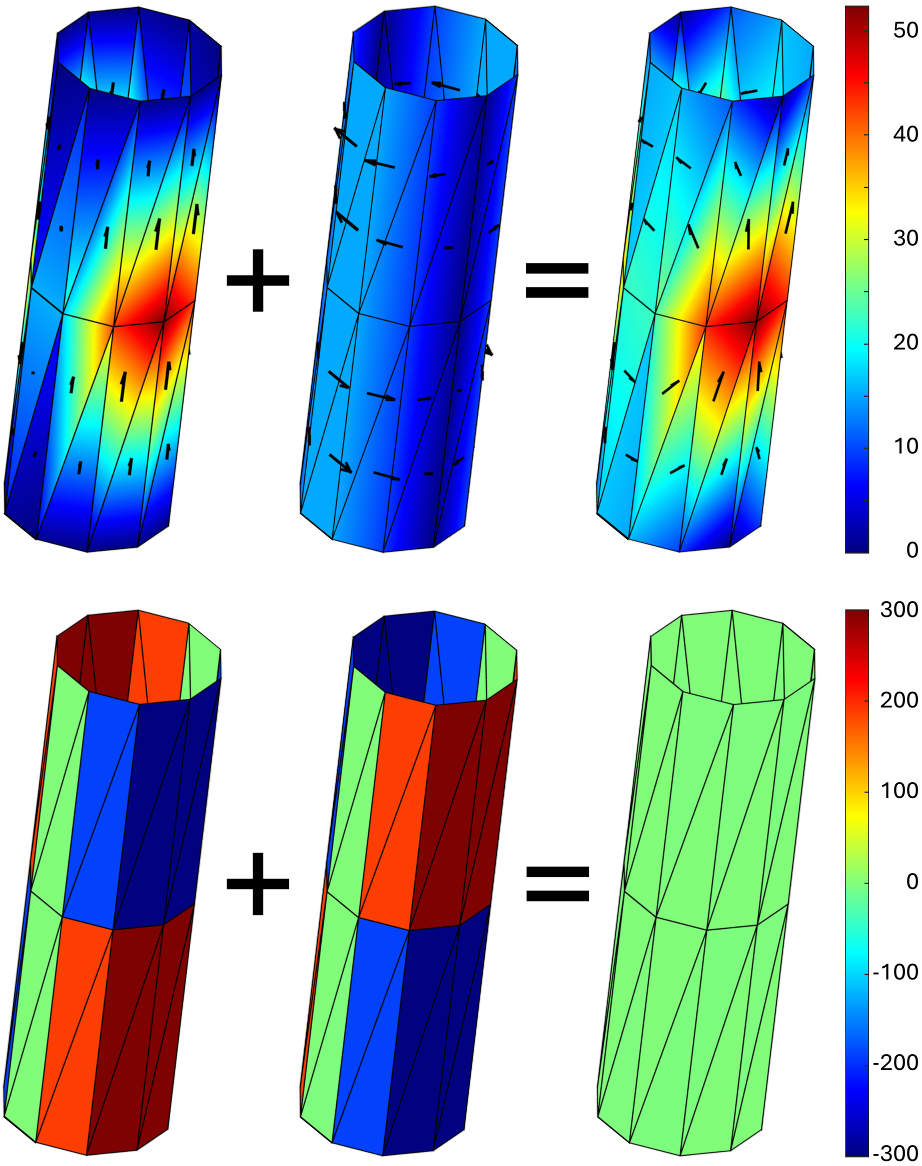

Figure 5: Sum of a cosinusoidally varying axial MBF and two sinusoidally varying circumferential MBFs, yielding solenoidal flow. Top: MBFs. Bottom: divergence of MBFs.

thin-wire MoM with tubular rooftop basis functions, as provided by FEKO [23], is used with axial discretization set equal to that of the MBF MoM meshes. Secondly, a hybrid TLT solver is used, as provided by FEKO, which FEKO labels its "multiconductor transmission line cable coupling" solver option. As noted in the introduction, the RWG MoM is used as reference to judge the accuracy of the other solutions. It employs the same surface meshes as the MBF solver. It is a widely used robust and trusted full-wave solution for general PEC surface geometries. All test geometries feature wires above an infinite PEC

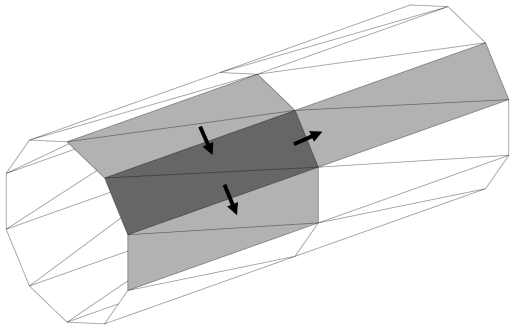

Figure 6: Contributions by an axial MBF at one edge, and a circumferential MBF at two edges, to current flow out of a quadrilateral, for the case in Fig. 5.

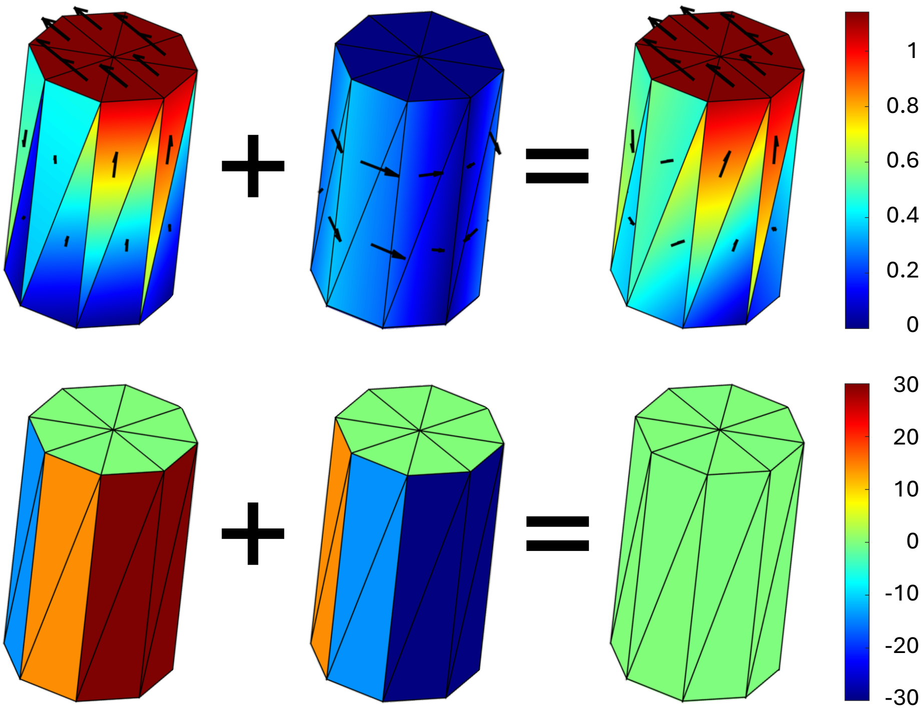

Figure 7: Sum of a cosinusoidally varying axial MBF flowing onto an end-cap, where it takes the form of a radial MBF, and a sinusoidally varying circumferential MBF, yielding solenoidal flow. Top: MBFs. Bottom: divergence of MBFs.

ground plane, which is a standard option in the commercial solvers; and is straightforwardly incorporated into the free space MoM formulation of (2) and (3) by accounting for image currents and excitations.

Tests #1 to #3 consider electrically thin wires over the band [100 MHz, 20 GHz], with strong proximity effects. The MBF solution meshes entail geometric circumferential discretization of $K = 10$ (K is defined in Section 2.1), and axial discretization of 0.675 mm, which corresponds to $\lambda/22$ meshing at 20 GHz. Test #4 evaluates the limit of MBF applicability as wires become electrically thick.

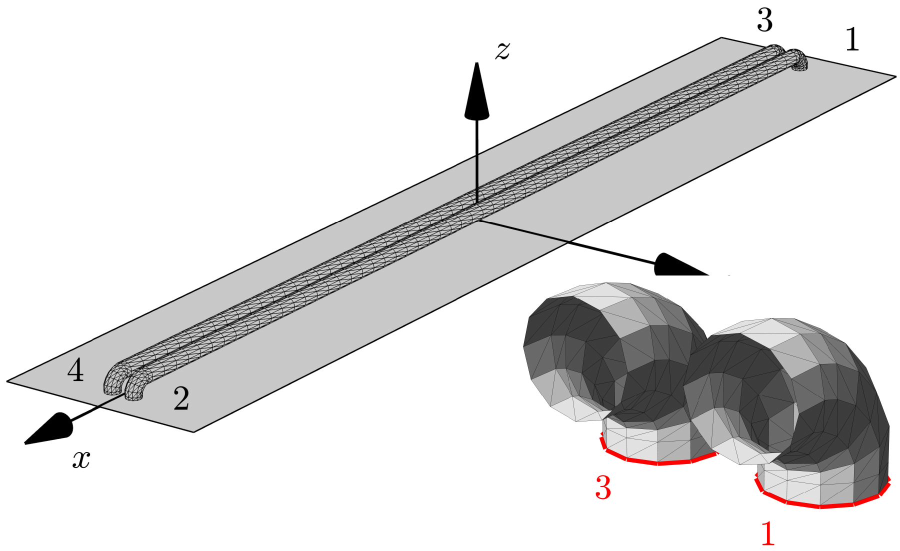

Figure 8: Test #1 – geometry. It is a three-conductor TL consisting of two parallel wires above a ground plane. The close-up view shows the near-end terminations to ground, as well as the port contours at which lumped loads and sources are placed. The far-end terminations are the same.

The number of DoFs required to represent current on a wire with MBFs, is five times fewer than with RWGs in the case of $K = 10$.

In all test cases, load values are chosen to approximately match TL characteristic impedances, since matching is often of engineering importance. However, the MBF solver accuracy performance demonstrated in this section is the same for arbitrary load values.

4.1 Test #1 – Parallel Wires Above Ground Plane

Consider two parallel wires of length 40 mm and radius 0.3 mm, with center-to-center distance of 0.9 mm. The wires are placed at the (center) height 0.6 mm above ground, as shown in Fig 8. Electrically, the wire lengths vary from 0.013λ to 2.7λ over the frequency range considered. An analytical but approximate analysis [17] based on line sources at the center lines and image theory yields a characteristic impedance matrix with diagonal entries $83\,\Omega$ and off-diagonal entries $31\,\Omega$. A more accurate analysis with EMEC [25] based on solving the cross-sectional boundary value problem (accounting for all proximity effects) yields the diagonal entries $75\,\Omega$ and the off-diagonal entries $26\,\Omega$. Both wires are terminated by quarter-circle wire arcs, where lumped sources and loads are applied at the interface with ground (see Fig. 8). In the MBF solution, MBFs are used for the wire parts that run parallel to the xy-plane, and RWGs for the quarter-circle wire arcs down to ground (this also applies to Test #2).

For crosstalk analysis, the aggressor wire is excited by a time-harmonic voltage source of amplitude 1 V at port 1 and terminated by a resistive load of $85\,\Omega$ at port 2. The victim wire is terminated by $85\,\Omega$ loads at both ends (ports 3 and 4). For the near-end (NE) and far-end (FE) of the TL, this yields the voltage

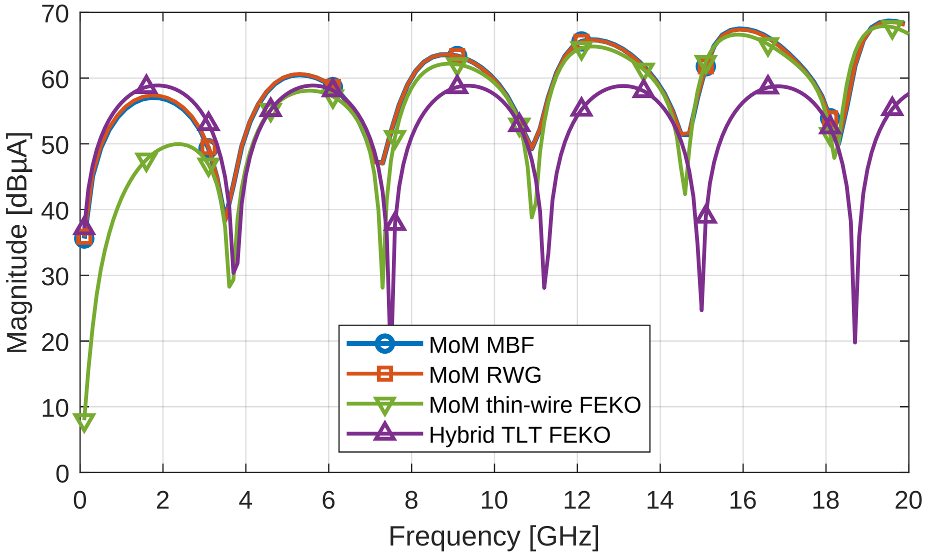

Figure 9: Test #1 – crosstalk. Induced current through the victim load resistor at port 4.

reflection coefficient matrices as

$$\mathbf{R}_{\mathrm{NE}} = \begin{bmatrix} -1 & 0 \\ -0.4 & 0.1 \end{bmatrix}, \quad \mathbf{R}_{\mathrm{FE}} = \begin{bmatrix} 0.1 & -0.2 \\ -0.2 & 0.1 \end{bmatrix}, \tag{23}$$

which are based on the more accurate characteristic impedance values. Fig. 9 shows the wideband far-end crosstalk (FEXT) current. The MBF solution agrees very well with the RWG reference. For this relatively basic test, both the thin-wire and hybrid TLT solvers yield results that do not agree with the reference solution over significant portions of the frequency band, and both underestimate the crosstalk current.

To study radiated immunity, port 1 is shorted and the problem is instead excited with a plane wave of amplitude $E_0 = 1\,\mathrm{V/m}$ incident from the direction $\phi = \theta = 45^\circ$ with a polarization angle of $\alpha = 45^\circ$. Fig. 10 defines incident plane wave characteristics as utilized throughout. Clearly, the incident plane wave corresponds to an aggressor source placed infinitely far from the victim. Fig. 11 shows the induced current through the FE load in the victim circuit. Again, the MBF solution agrees very well with the reference. The hybrid TLT solution is increasingly inaccurate as the frequency is raised. The thin-wire solution predicts the induced current relatively well. The latter is attributed to the incident plane wave providing a distributed excitation of the problem that is more compatible with the thin-wire approximation, in contrast to the voltage source's excitation of a strong current on the aggressor line in combination with proximity effects.

For this test, the RWG solution requires 4460 DoFs, the MBF solution requires 1560 DoFs and the thin-wire solution requires 170 DoFs. For N DoFs, direct linear system solution runtime and memory requirement scale as N^3 and N^2, respectively. In this instance, the MBF solver thus reduces runtime by a factor 23 and memory requirement by a factor 8, as compared to the RWG

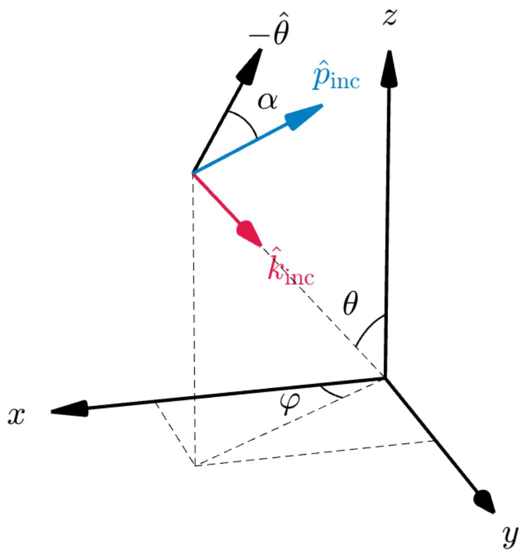

Figure 10: The electric field of an incident plane wave is defined as $\boldsymbol{E}_{\mathrm{inc}} = \hat{p}_{\mathrm{inc}} E_0 \exp(-jk_0 \hat{k}_{\mathrm{inc}} \cdot \boldsymbol{r})$. The direction of propagation unit vector $\hat{k}_{\mathrm{inc}}$, is defined in terms of the standard spherical coordinate system angles (θ, ϕ), as shown. The polarization unit vector is rotated by an angle α relative to $-\hat{\theta}$, such that $\hat{p}_{\mathrm{inc}} = -\cos\alpha\hat{\theta} + \sin\alpha\hat{\phi}$.

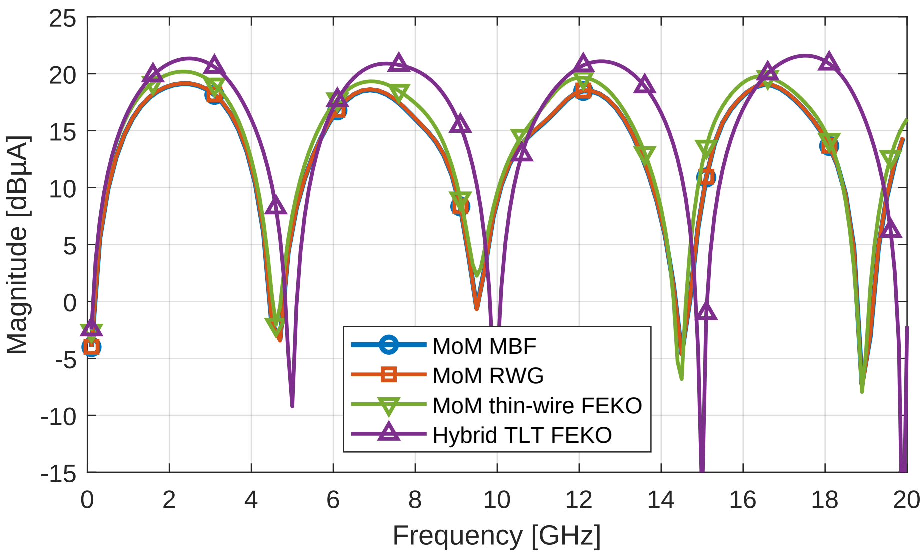

Figure 11: Test #1 – radiated immunity. Induced current through the victim load resistor at port 4.

solver, while yielding essentially identical results.

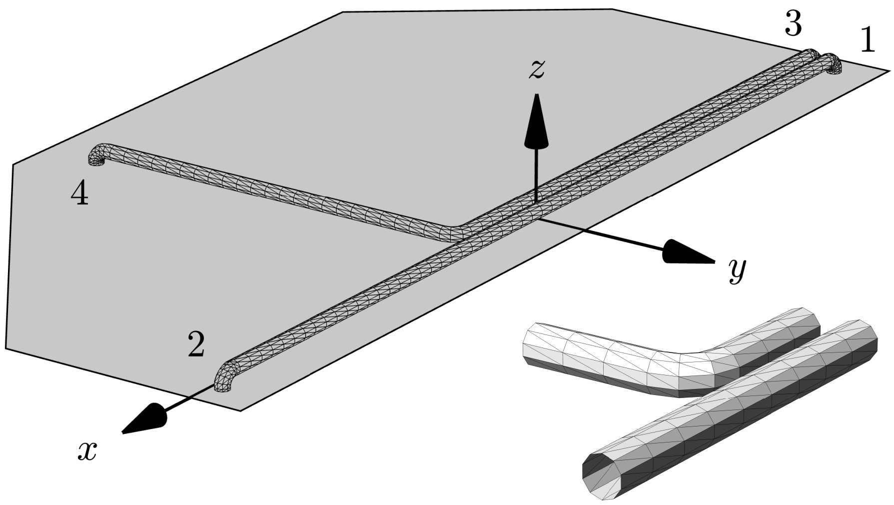

Figure 12: Test #2 – geometry. It is a three-conductor TL consisting of two wires above a ground plane, where the agressor wire (from ports 1 to 2) is straight and the victim wire (from ports 3 to 4) is L-shaped. A zoomed-in view of the bend geometry is shown. The close-up view in Fig. 8 also applies here, showing the near-end terminations to ground, as well as the port contours at which lumped loads and sources are placed. The port 2 and 4 terminations and contours are entirely similar.

4.2 Test #2 – L-shaped Victim Wire Above Ground Plane

Now consider a variation on the Test #1 setup, as shown in Fig. 12. Here, the 40 mm long aggressor wire is as before, but the victim wire is bent to form a 90° L-shape. The centerline of the victim's orthogonal section aligns with the 25 mm position along the aggressor's length, and the orthogonal section extends to 15 mm away from the extended centreline of its parallel section. The wire radii, distances above ground, parallel spacing and terminations to ground, are the same as for Test #1. For the wires connected to ports 2 and 4 the characteristic impedance is 79 Ω, based on the exact solution to a circular conductor above ground.

For crosstalk analysis, a 1 V source is placed at port 1 and an 85 Ω load at port 2, for the aggressor wire. The victim wire is terminated by 85 Ω resistive loads at ports 3 and 4. Thus, the voltage reflection coefficient is 0.04 at both ports 2 and 4, and the voltage reflection coefficient matrix $\mathbf{R}_{\mathrm{NE}}$ in (23) applies to ports 1 and 3. Fig. 13 shows the magnitude of the FEXT current at port 4. Again, the MBF solution is seen to agree very well with the RWG reference. The thin-wire solution fails to agree with the reference, and the magnitude of the FEXT current is underestimated for most frequencies considered, by up to about 20 dB. The hybrid TLT solver is only accurate in the low-frequency limit, and generally exhibits frequency variation that lacks many of the finer details of the reference solution.

For radiated immunity, Fig. 14 shows the current through the resistor at port 4 when port 1 is shorted and the problem is excited with a plane wave of

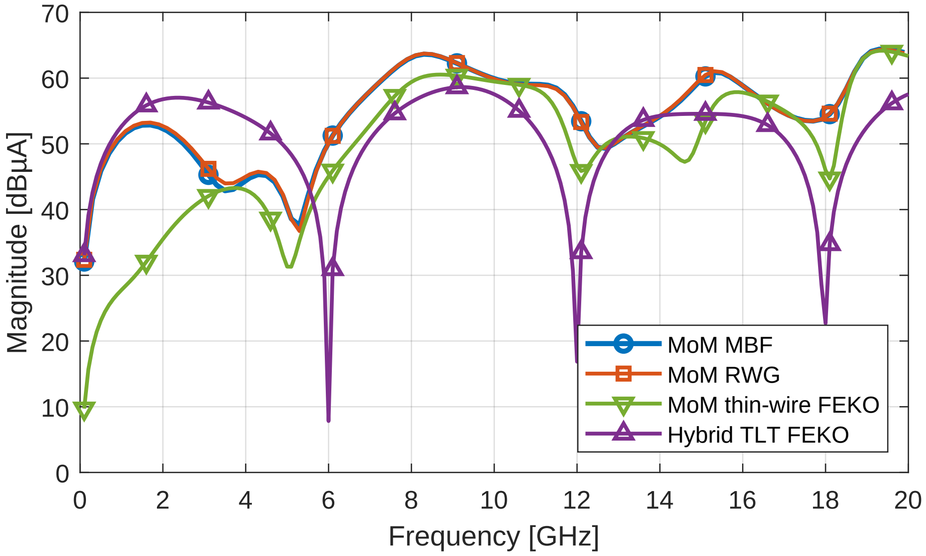

Figure 13: Test #2 – crosstalk. Induced current through the victim load resistor at port 4.

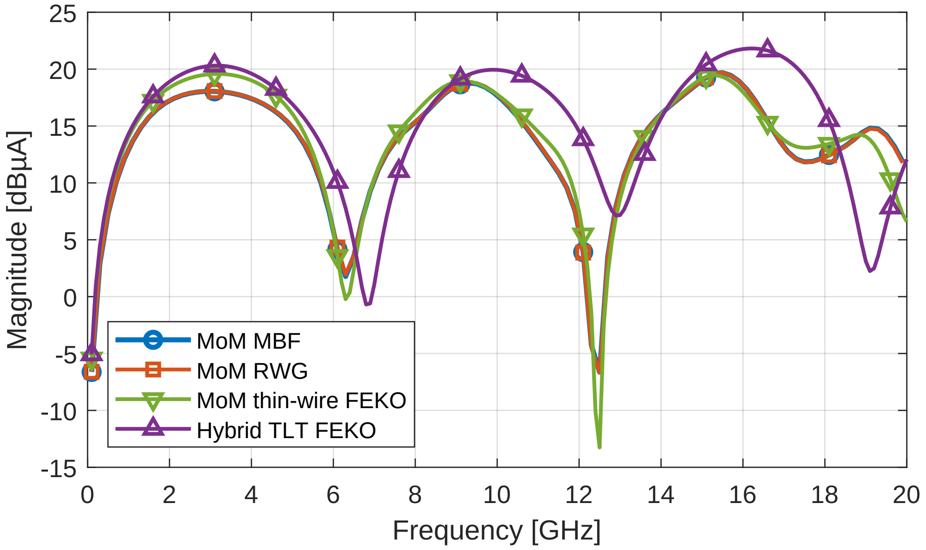

Figure 14: Test #2 – radiated immunity. Induced current through the victim load resistor at port 4.

amplitude $E_0 = 1\,\mathrm{V/m}$, incident from the direction $\phi = \theta = 45°$ with polarization angle $\alpha = 45°$. The MBF solution consistently agrees with the reference solution throughout the frequency band. As for Test #1, the hybrid TLT solution fails to predict the current through the resistor at port 4 (except in the low-frequency limit), whereas the thin-wire solution shows better agreement and this is again attributed to the characteristics of the plane wave excitation as compared to the voltage source excitation as discussed for Test #1.

The RWG solution requires 4520 DoFs, the MBF solution requires 1578 DoFs and the thin-wire solution requires 164 DoFs. These numbers are very similar to those of Test #1; again, the MBFs yield a very significant efficiency improvement over the RWGs, while the other two solvers are not able to solve the problem reliably.

4.3 Test #3 – Twisted-Pair Victim Transmission Line

This test entails a twisted-pair victim TL that is placed in close proximity and parallel to a straight aggressor wire as shown in Fig. 15. Both TLs have length 40 mm. All wires have radius 0.3 mm, as before. The aggressor connects ports 1 and 2. The height of its horizontal part's centerline is 1.2 mm above ground. The twisted-pair TL, connecting ports 3 and 4, is constructed from two helix-shaped wires. The combined bifilar helix have 13 turns such that there are no "half-twists" that could increase coupling to an external field [1]. The radius of the bifilar helix is 0.6 mm (from the center contours of the wires to the helix's centerline), where the helix's centerline runs 1.2 mm above the ground plane and is spaced 1.5 mm from the aggressor's centerline. The aggressor is terminated to ground with port contours at the intersections, similar to the previous test cases. At both ends of the twisted pair it terminates on itself through half-circle wire arcs with port contours placed in a balanced fashion, as illustrated in Fig. 15. The midpoints of the half-circle wire arcs are connected to ground by vertical wires to improve immunity to capacitive coupling [2]. The balanced ports of the twisted pair allow for straightforward computation of differential- and common-mode currents.

For the MBF solution, MBFs are employed to represent the surface current on the straight part of the aggressor and on the victim's two helix-shaped wires. RWGs are used for the victim's two half-circle wire arcs, as well as all terminations down to ground (see Fig. 15). This again illustrates the flexibility and power of the proposed method, allowing for efficient surface-current modeling by MBFs on the long and relatively homogeneous wire sections which would otherwise require a high number of DoFs, in seamless combination with rigorous surface-current modeling via RWGs for intricate geometrical details at the terminations.

The aggressor wire has a characteristic impedance of about 120 Ω, which is based on analytical expressions and image theory (where the victim's presence is ignored). Ports 2, 3 and 4 are each connected to a 120 Ω resistive load. A 1 V source is connected to port 1. Fig. 16 shows the magnitude of the FEXT differential-mode and common-mode current, where the loads on the victim line are implemented in a balanced fashion with respect to the grounding connections at the half-circle wire arc midpoints. Again, the MBF solution agrees very well with the RWG reference. The thin-wire solution fails to reproduce the reference solution in the same consistent fashion, where it underestimates the FEXT current in places, by up to almost 20 dB. The hybrid TLT solution exhibits even larger deviations and is not usable at higher frequencies. Although, as expected, it becomes accurate in the low-frequency limit, as radiative effects diminish and ultimately disappear. Note that the hybrid TLT solver does incorporate the additional length of the helix-shaped wires caused by the twisting. For comparison, Fig. 17 shows the corresponding results for unbalanced loading of the victim wire, where one of the helix-shaped wires is terminated by 120 Ω

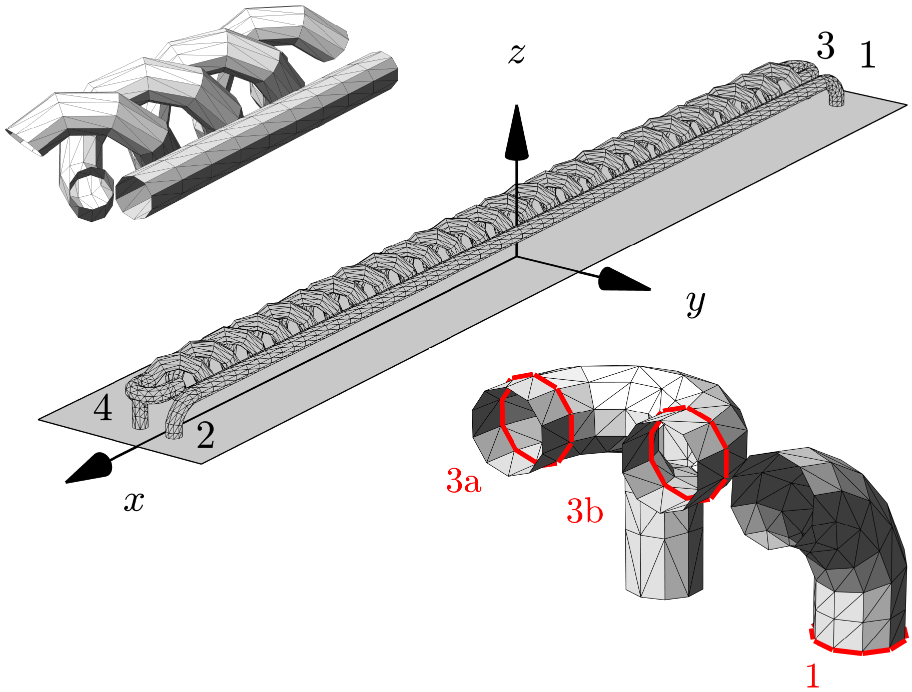

Figure 15: Test #3 – geometry. The straight aggressor wire is in close proximity to the twisted-pair victim TL, above ground. At the top a zoomed-in view of the TL meshing is shown. The bottom close-up view shows the near-end terminations and port contours. The aggressor is terminated to ground, while the victim twisted pair terminates on itself, while also being grounded. Note the balanced configuration of port 3, which consists of contours 3a and 3b. The far-end terminations are the same.

resistive loads at both ends and the other with zero resistive loading. Similar observations hold, for the relative performances of the solvers. A comparison of Fig. 17 with Fig. 16 shows the significant reduction in FEXT current achieved through balanced loading of the victim TL.

Now consider radiated immunity given a victim twisted-pair with balanced loads. Port 1 is again shorted. Fig. 18 shows the magnitudes of the differential-mode and common-mode current through port 4. The problem is excited with a plane wave incident from $\phi = \theta = 45°$ with polarization angle $\alpha = 45°$. For comparison, Fig. 19 shows the corresponding results for unbalanced loading at ports 3 and 4. Again, the MBF solution reproduces the reference solution consistently in all cases, whereas the thin-wire solution fails to do so for some parts of the frequency band to varying degrees. The hybrid TLT solution fails to a much larger extent, to reproduce the reference solution.

For this problem, the RWG solution requires 8903 DoFs, the MBF solution requires 2731 DoFs and the thin-wire solution requires 301 DoFs. In this case, for a direct solution, the MBF solver reduces runtime by a factor 35 and memory requirement by a factor 11, compared to the RWG solver, which are the only reliable solvers.

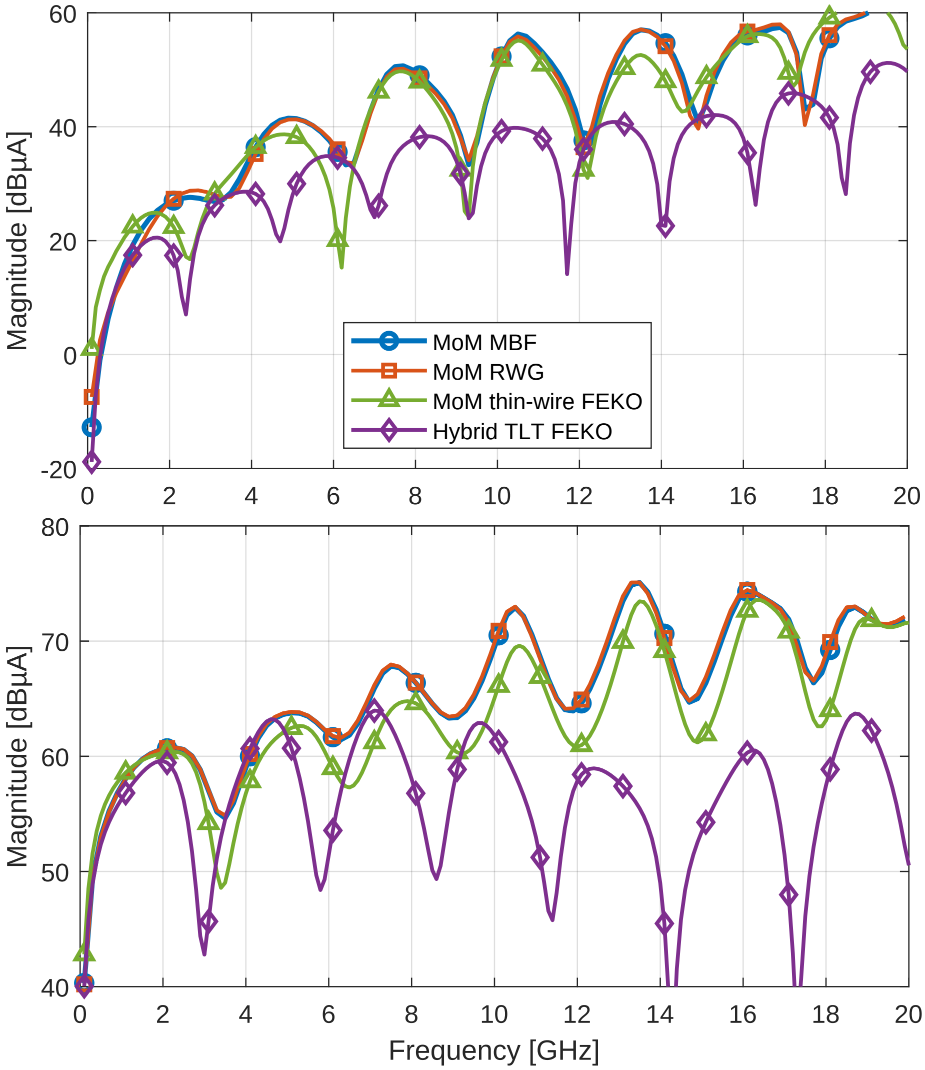

Figure 16: Test #3 – crosstalk. Induced current at port 4 for the victim TL with balanced loads. Top: differential mode. Bottom: common mode.

4.4 Test #4 – Electrically Thick Parallel Wires

This final test considers the accuracy of the FEXT current in a band where the wire electrical radius transitions from thin to thick. The physical setup is the same as in Test #1 (see Section 4.1), except that the lengths of the parallel lines are reduced by a factor of ten, to 4 mm. The test band is changed to [10 GHz, 300 GHz], corresponding to electrical wire radius range $[0.01\lambda, 0.3\lambda]$, circumference range $[0.063\lambda, 1.9\lambda]$, and length range $[0.13\lambda, 4\lambda]$. Circumferential discretization of $K = 20$ is used and axial discretization of 0.1 mm, which corresponds to $\lambda/10$ meshing of the wire surfaces at 300 GHz, ensuring that the RWG reference solution is not under discretized in terms of elements per wavelength.

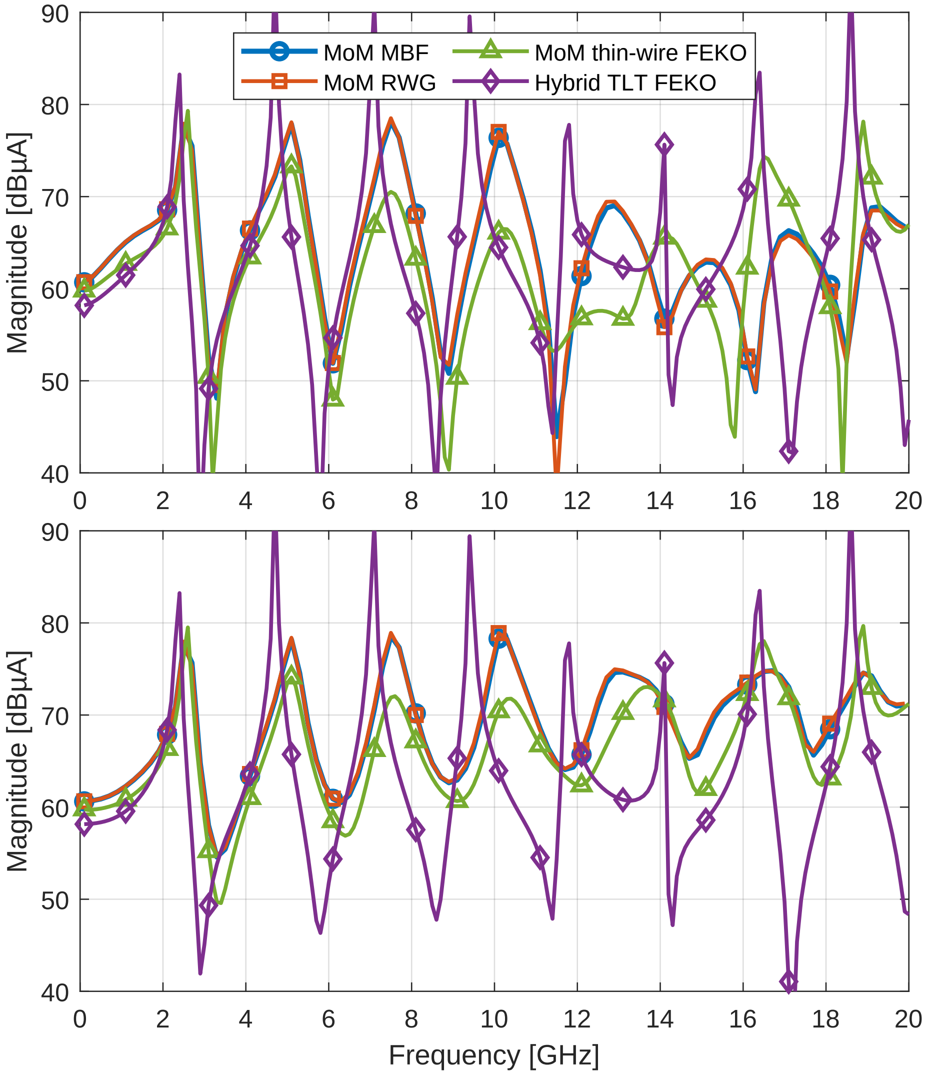

Figure 17: Test #3 – crosstalk. Induced current at port 4 for the victim TL with unbalanced loads. Top: differential mode. Bottom: common mode.

Let I_{RWG} denote the RWG reference FEXT current, and I_{test} a solution with one of the other methods. The percentage relative error in I_{test} is defined as

$$\mathrm{Error} = \frac{|I_{\mathrm{test}} - I_{\mathrm{RWG}}|}{|I_{\mathrm{RWG}}|} \times 100\%. \tag{24}$$

Fig. 20 shows the results. The FEKO hybrid TLT solver does not compute results for TLs with cross sectional electrical dimensions above certain limits due to exceedingly poor satisfaction of TLT assumptions, hence no results are shown beyond 100 GHz. As expected, this approach is completely unsuitable in the high-frequency regime considered. The thin-wire solution is generally significantly less accurate than the MBF solution, and diverges dramatically from the reference in the upper half of the band. The MBF solution follows the

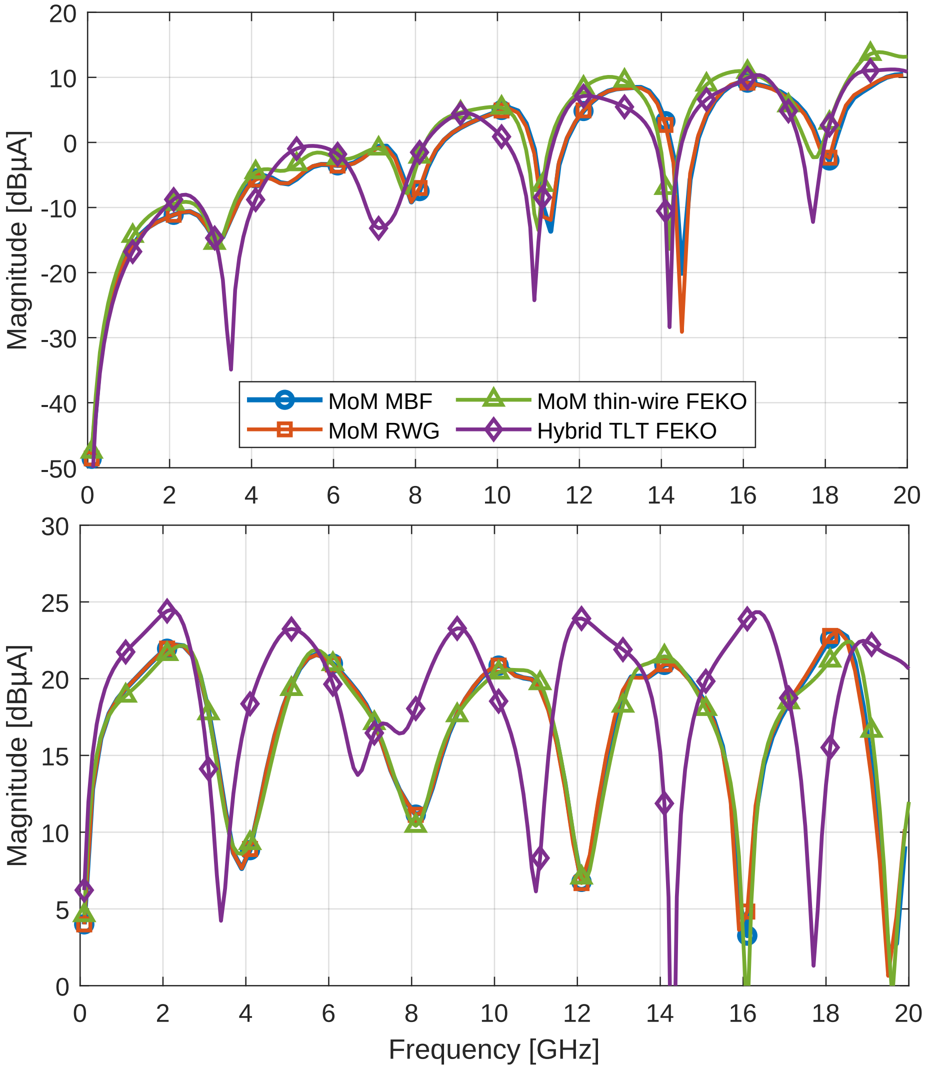

Figure 18: Test #3 – radiated immunity. Induced current at port 4 for the victim TL with balanced loads. Top: differential mode. Bottom: common mode.

reference very closely, until a slow decline in accuracy sets in over the upper half of the band, starting at $a \approx 0.15\lambda$. This decline is due to under discretization in terms of circumferential harmonic order. At this radius the wire circumference is about one wavelength. Whereas the MBFs show graceful degradation as under discretization sets in, the thin-wire solver becomes completely unsuitable. The observed MBF under-discretization onset corresponds well with unstabilized MBF results from [7].

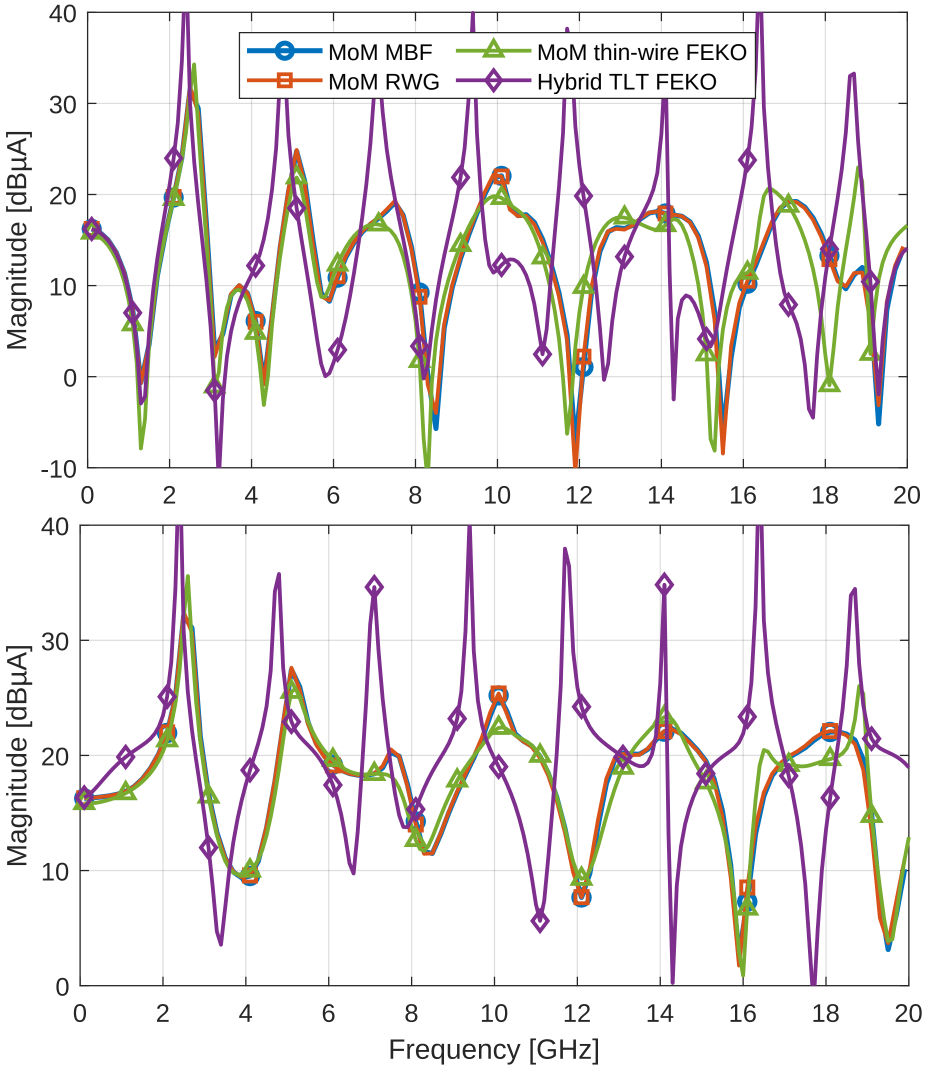

Figure 19: Test #3 – radiated immunity. Induced current at port 4 for the victim TL with unbalanced loads. Top: differential mode. Bottom: common mode.

5 Conclusion

Stabilized MBFs for wire current modeling are presented, which are constructed from standard basis functions used to represent surface current density in the MoM on triangle element meshes. Stabilization is achieved by constructing the MBFs in such a way that solenoidal current flow can be represented exactly, which eradicates the occurrence of spurious solutions. The MBFs represent axial and circumferential current components and variations along wires, and radial and azimuthal components and variations at end-caps. Crosstalk and radiated immunity results for TL geometries of varying complexity, show that the MBF MoM solver is very well suited to wideband analysis of cases featur-

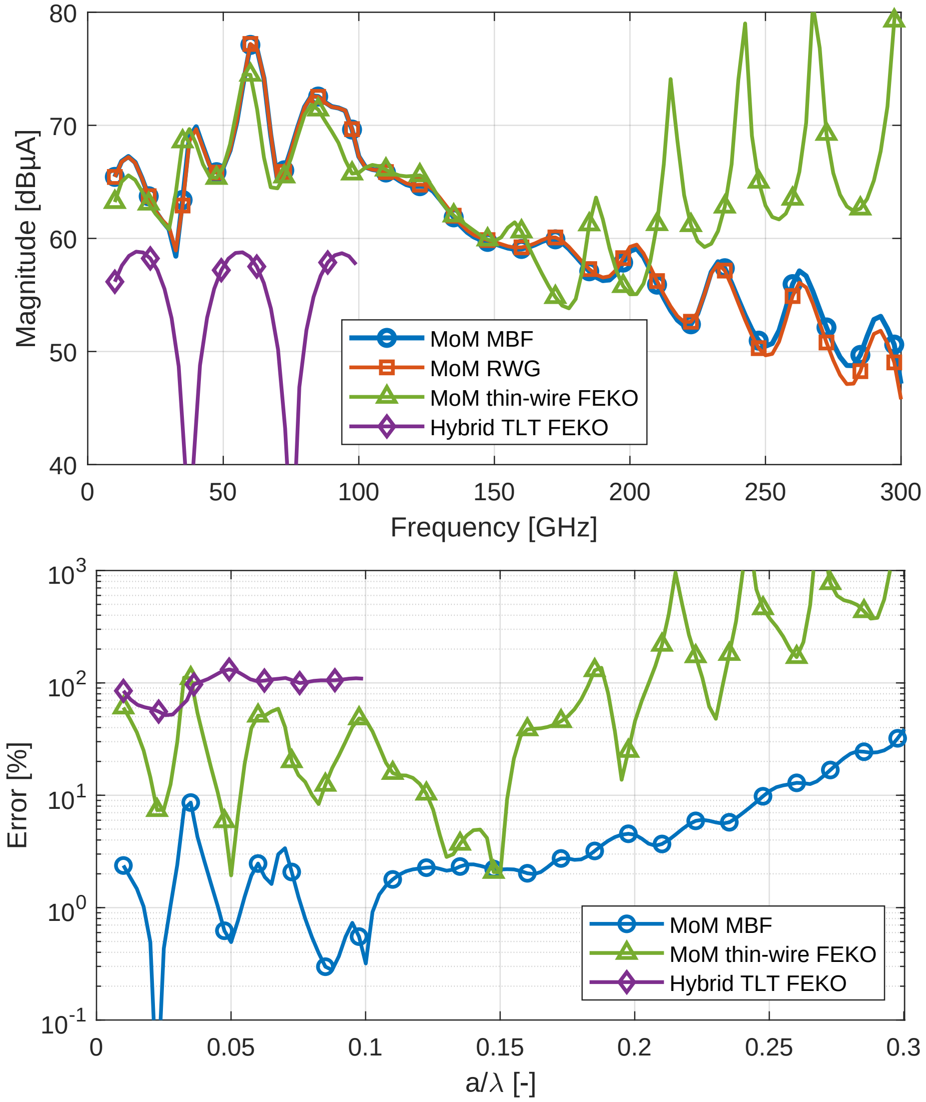

Figure 20: Test #4 – crosstalk. Top: induced current through the victim load resistor at port 4. Bottom: percentage relative error in the crosstalk current, with the RWG MoM as reference.

ing strong proximity and radiative effects. Results show that the MBFs are accurate up to electrically thick radii of $a \lesssim 0.15\lambda$, with graceful degradation in accuracy as the thickness is increased further. The MBFs support seamless integration with external geometry, enabling rigorous modeling of intricate wire junctions. Accuracy for antenna analysis with the unstabilized MBFs has been demonstrated before, in [7]. The results show that existing formulations tailored to wire analysis, namely thin-wire MoM and hybrid TLT solutions, are generally not reliable for wire coupling analysis and can significantly underestimate crosstalk and irradiation-induced signals over unpredictable frequency ranges. In complex applications, physical insight for quantitative estimation of expected behavior becomes very difficult, which makes a trustworthy solver essential. Among such solvers the MBF MoM is the most efficient, to the authors' knowledge. Computational cost savings relative to the benchmark RWG MoM are significant (see also [7]), with MBFs producing essentially identical solutions. For fixed computational resources, this means that significantly larger problems may be solved and wider ranges of design options may be explored.

Additional MBFs can be formulated to represent higher-order circumferential variations, i.e. $\cos 2\varphi$, $\sin 2\varphi$, etc., but in all test cases considered here and in [7], there are little room for further improvement of port parameter accuracy. Such MBFs could be relevant for high-precision current density computations (but should be weighed against switching to LBFs), or to extend the range of applicability to even electrically thicker wires. Finite conductivity can be incorporated into the MBF solver with an impedance boundary condition (see [35]). The test cases considered here involve wire-like external geometries (the terminations to ground), but the solver supports general external geometry, e.g. the chassis of a motor vehicle. The MBFs can be used for transient analysis by computing a wideband response with the frequency domain MoM and inverse Fourier transforming to the time domain, as e.g. in [36, 37]. Alternatively, their incorporation into time-domain MoM solvers could be explored [38, 39].

References

[1] C. R. Paul, R. C. Scully, and M. A. Steffka, *Introduction to Electromagnetic Compatibility*, 3rd ed. Hoboken, NJ: John Wiley & Sons, 2023.

[2] H. W. Ott, *Electromagnetic Compatibility Engineering.* Hoboken, NJ: John Wiley & Sons, 2009.

[3] W. A. Radasky and M. Bäckström, "Brief historical review and bibliography for intentional electromagnetic interference (IEMI)," in *Proceedings of the XXXIth URSI General Assembly and Scientific Symposium (URSI GASS)*, 2014, pp. 1–4.

[4] W. A. Radasky and R. Hoad, "Recent developments in high power EM (HPEM) standards with emphasis on high altitude electromagnetic pulse (HEMP) and intentional electromagnetic interference (IEMI)," *IEEE Letters on Electromagnetic Compatibility Practice and Applications*, vol. 2, no. 3, pp. 62–66, 2020.

[5] G. Andrieu, L. Koné, F. Bocquet, B. Démoulin, and J.-P. Parmantier, "Multiconductor reduction technique for modeling common-mode currents on cable bundles at high frequency for automotive applications," *IEEE Transactions on Electromagnetic Compatibility*, vol. 50, no. 1, pp. 175–184, 2008.

[6] A. Schröder, G. A. Rasek, H.-D. Brüns, Z. Řezníček, J. Kučera, S. E. Loos, and C. Schuster, "Analysis of high intensity radiated field coupling into aircraft using the method of moments," *IEEE Transactions on Electromagnetic Compatibility*, vol. 56, no. 1, pp. 113–122, 2014.

[7] W. R. Dommisse, J. T. Du Plessis, P. I. Cilliers, M. M. Botha, and T. Rylander, "Macro basis functions for efficient analysis of thick wires in the

MoM," *IEEE Transactions on Antennas and Propagation*, vol. 72, no. 7, pp. 5865–5876, 2024.

[8] D. H. Werner, "A Method of Moments Approach for the Efficient and Accurate Modeling of Moderately Thick Cylindrical Wire Antennas," *IEEE Transactions on Antennas and Propagation*, vol. 46, no. 3, pp. 373–382, 1998.

[9] A. M. A. Jalloul and J. L. Young, "Singularity evaluation of the straight-wire mixed-potential integral equation in the method of moments procedure," *IEEE Transactions on Antennas and Propagation*, vol. 59, no. 1, pp. 172–179, 2011.

[10] D. B. Davidson, "Convergence of the MPIE Galerkin MoM thin wire formulation," *IEEE Transactions on Antennas and Propagation*, vol. 69, no. 10, pp. 7073–7078, 2021.

[11] G. Fikioris and T. T. Wu, "On the application of numerical methods to Hallen's equation," *IEEE Transactions on Antennas and Propagation*, vol. 49, no. 3, pp. 383–392, 2001.

[12] A. Heldring and J. Rius, "Efficient full kernel calculation for wire antennas," in *Proceedings of IEEE International Symposium on Antennas and Propagation (IEEE AP-S)*, vol. 4, 2004, pp. 3461–3464.

[13] A. Mohan and D. S. Weile, "Accurate modeling of the cylindrical wire kernel," *Microwave and Optical Technology Letters*, vol. 48, no. 4, pp. 740–744, 2006.

[14] D. R. Wilton and N. J. Champagne, "Evaluation and integration of the thin wire kernel," *IEEE Transactions on Antennas and Propagation*, vol. 54, no. 4, pp. 1200–1206, 2006.

[15] E. Forati, A. D. Mueller, P. Gandomkar Yarandi, and G. W. Hanson, "A new formulation of Pocklington's equation for thin wires using the exact kernel," *IEEE Transactions on Antennas and Propagation*, vol. 59, no. 11, pp. 4355–4360, 2011.

[16] F. M. Tesche, M. V. Ianoz, and T. Karlsson, *EMC Analysis Methods and Computational Models*. New York, NY: John Wiley & Sons, 1997.

[17] C. R. Paul, *Analysis of Multiconductor Transmission Lines*, 2nd ed. Hoboken, NJ: John Wiley & Sons, 2008.

[18] C. A. Nucci and F. Rachidi, "On the contribution of the electromagnetic field components in field-to-transmission line interaction," *IEEE Transactions on Electromagnetic Compatibility*, vol. 37, no. 4, pp. 505–508, 1995.

[19] S. Chabane, "A modified enhanced transmission line theory as a solution to wiring configurations inconsistent with the classical transmission line theory - Application to vehicle harnesses," Ph.D. dissertation, INSA de Rennes, France, 2014.

[20] S. Chabane, P. Besnier, and M. Klingler, “A modified enhanced transmission line theory applied to multiconductor transmission lines,” *IEEE Transactions on Electromagnetic Compatibility*, vol. 59, no. 2, pp. 518–528, 2017.

[21] Y. Wang, Y. S. Cao, D. Liu, R. W. Kautz, N. Altunyurt, and J. Fan, “Evaluating the crosstalk current and the total radiated power of a bent cable harness using the generalized MTL method,” *IEEE Transactions on Electromagnetic Compatibility*, vol. 62, no. 4, pp. 1256–1265, 2020.

[22] D. Tashiro, T. Hisakado, T. Matsushima, and O. Wada, “Single-conductor transmission line model incorporating radiation reaction,” *IEEE Transactions on Electromagnetic Compatibility*, vol. 63, no. 4, pp. 1065–1077, 2021.

[23] Altair, *FEKO*, 2022. [Online]. Available: https://www.altair.com/feko/

[24] Dassault Systèmes, *SIMULIA – CST Studio Suite*, 2025. [Online]. Available: https://www.3ds.com/products/simulia/cst-studio-suite/

[25] J. Carlsson, T. Karlsson, and G. Undén, “EMEC – an EM simulator based on topology,” *IEEE Transactions on Electromagnetic Compatibility*, vol. 46, no. 3, pp. 353–358, 2004.

[26] J.-M. Jin, *Theory and Computation of Electromagnetic Fields.* New York: John Wiley and Sons, 2010.

[27] J. Heinstadt, “New approximation technique for current distribution in microstrip array antennas,” *Electronics Letters*, vol. 21, no. 29, pp. 1809–1810, 1993.

[28] E. Suter and J. R. Mosig, “A subdomain multilevel approach for the efficient MoM analysis of large planar antennas,” *Microwave and Optical Technology Letters*, vol. 26, no. 4, pp. 270–277, 2000.

[29] J. Wang and J. P. Webb, “Hierarchal vector boundary elements and p-adaption for 3-D electromagnetic scattering,” *IEEE Transactions on Antennas and Propagation*, vol. 45, no. 12, pp. 1869–1879, December 1997.

[30] J. P. Webb, “Hierarchal vector basis functions of arbitrary order for triangular and tetrahedral finite elements,” *IEEE Transactions on Antennas and Propagation*, vol. 47, no. 8, pp. 1244–1253, August 1999.

[31] ——, “Edge elements and what they can do for you,” *IEEE Transactions on Magnetics*, vol. 29, no. 2, pp. 1460–1465, 1993.

[32] D. Sun, J. Manges, X. Yuan, and Z. Cendes, “Spurious modes in finite-element methods,” *IEEE Antennas and Propagation Magazine*, vol. 37, no. 5, pp. 12–24, 1995.

[33] J.-M. Jin, *The Finite Element Method in Electromagnetics*, 3rd ed. John Wiley & Sons, 2014.

[34] V. De la Rubia, D. Young, G. Fotyga, and M. Mrozowski, “Spurious modes in model order reduction in variational problems in electromagnetics,” *IEEE Transactions on Microwave Theory and Techniques*, vol. 70, no. 11, pp. 5159–5171, 2022.

[35] W. R. Dommisse, M. M. Botha, and T. Rylander, "Modelling of thick conducting wires with macro basis functions," in *Proceedings of the IEEE International Symposium on Antennas and Propagation (IEEE AP-S)*. IEEE, 2024, pp. 1353–1354, Florence, Italy.

[36] D. I. Olcan and B. M. Kolundzija, "Computation of time-domain responses via frequency-domain analysis and FFT," in *Proceedings of the International Symposium on Antennas and Propagation (ISAP)*, 2007, pp. 1031–1034, Niigata, Japan.

[37] R. Moini, M. Nazari, S. Fortin, and F. P. Dawalibi, "On the use of the antenna theory model of lightning return stroke with distributed current source for EMC analysis," *IEEE Transactions on Electromagnetic Compatibility*, vol. 61, no. 3, pp. 674–680, 2019.

[38] B. P. Rynne, "Time domain scattering from arbitrary surfaces using the electric field integral equation," *Journal of Electromagnetic Waves and Applications*, vol. 5, no. 1, pp. 93–112, 1991.

[39] G. Iwasa, E. Gad, and D. A. McNamara, "TD-EFIE method-of-moments solution using the numerical inversion of the Laplace transform with time-stepping re-initialization," *IEEE Transactions on Antennas and Propagation*, vol. 72, no. 11, pp. 8655–8668, 2024.